Evidence for C and Mg variations in the GD-1 stellar stream

Balbinot, Eduardo; Cabrera-Ziri, Ivan; Lardo, Carmela

Published in:
Monthly Notices of the Royal Astronomical Society

DOI:
10.1093/mnras/stac1953

Publication date:
2022

Monthly Notices of the ROYAL ASTRONOMICAL SOCIETY

MNRAS **515,** 5802–5812 (2022) https://doi.org/10.1093/mnras/stac1953
Advance Access publication 2022 July 11

Evidence for C and Mg variations in the GD-1 stellar stream

Eduardo Balbinot [1]★ Ivan Cabrera-Ziri [2] and Carmela Lardo [3]

[1]*Kapteyn Astronomical Institute, University of Groningen, Landleven 12, NL-9747 AD Groningen, the Netherlands*
[2]*Astronomisches Rechen-Institut, Zentrum für Astronomie der Universität Heidelberg, Mönchhofstraße 12-14, D-69120 Heidelberg, Germany*
[3]*Dipartimento di Fisica e Astronomia, Università degli Studi di Bologna, Via Gobetti 93/2, I-40129, Bologna, Italy*

Accepted 2022 July 7. Received 2022 July 7; in original form 2021 November 24

ABSTRACT

Dynamically cold stellar streams are the relics left over from globular cluster dissolution. These relics offer a unique insight into a now fully disrupted population of ancient clusters in our Galaxy. Using a combination of *Gaia* eDR3 proper motions, optical and near-UV colours, we select a sample of likely Red Giant Branch stars from the GD-1 stream for medium-low resolution spectroscopic follow-up. Based on radial velocity and metallicity, we are able to find 14 new members of GD-1, 5 of which are associated with the *spur* and *blob/cocoon* off-stream features. We measured C-abundances to probe for abundance variations known to exist in globular clusters. These variations are expected to manifest in a subtle way in globular clusters with such low masses ($\sim 10^4$ $M_\odot$) and metallicities ([Fe/H] ~ -2.1 dex). We find that the C-abundances of the stars in our sample display a small but significant (3σ level) spread. Furthermore, we find $\sim 3\sigma$ variation in Mg-abundances among the stars in our sample that have been observed by APOGEE. These abundance patterns match the ones found in Galactic globular clusters of similar metallicity. Our results suggest that GD-1 represents another fully disrupted low-mass globular cluster where light-element abundance spreads have been found.

Key words: globular clusters: general – Galaxy: structure.

1 INTRODUCTION

Among the myriad of substructures present in the Milky Way (MW) halo, stellar streams stand out as being spatial and kinematic cohesive structures which in some cases span hundreds of degrees on the sky. In recent years, dozens of new streams have been discovered (e.g. Balbinot et al. 2016; Bernard et al. 2016; Malhan, Ibata & Martin 2018; Shipp et al. 2018; Ibata, Malhan & Martin 2019), and the community has exploited their properties to refine our knowledge about the mass and shape of the Galaxy as well as its accretion history (e.g. Küpper et al. 2015; Bonaca & Hogg 2018; Massari, Koppelman & Helmi 2019).

Streams are classified as *hot* or *cold* based on the dynamical temperature (i.e. velocity dispersion) of their progenitor. The low-velocity dispersion of their progenitor makes *cold* stellar streams intrinsically thin ($\lesssim$100 pc), pointing to globular clusters (GCs) as their precursors. Palomar 5 offers a spectacular example of a *cold* stream with tidal tails radiating from a still-bound cluster (e.g. Odenkirchen et al. 2001). However, in our Galaxy, *cold* streams like Palomar 5 are rare.

In fact, in the MW, most cold streams are progenitor-less (e.g. Shipp et al. 2018). This means that their GC progenitors are now completely dissolved. Yet, the vast majority of GCs in the Galaxy show no signs of having streams in formation (e.g. Kuzma, Da Costa & Mackey 2018; Sollima 2020).

It is natural to ask the origin of such a disparity between the numbers of GC with streams and progenitor-less cold streams. It is entirely possible that the GCs that gave rise to the population of progenitor-less streams were sampled from a distribution of long-gone GCs that differ from present-day MW GCs. One way of producing these fast-dissolving GCs is by retaining a large fraction of stellar-mass black holes, as demonstrated by Gieles et al. (2021). The authors propose two natural pathways: a low initial density or a flatter initial mass function; as well as nurture pathways, such as tidal heating and mass stripping during accretion. In this context, progenitor-less streams could be probing a population of intrinsically distinct GCs rather than the present-day ones in the MW. Alternatively, their progenitors may have formed in a host galaxy that is now accreted into the MW. In any of these cases, studying their remnants (stellar streams) may provide insight into the population of GCs no longer available in our Galaxy.

Although historically described as simple stellar populations, in reality, GCs are far from it. The abundances of light elements like e.g. He, C, N, and O are known to change from star to star within a cluster (e.g. Charbonnel 2016; Gratton et al. 2019). These multiple stellar populations (MPs) seem ubiquitous in high mass GCs ($\gtrsim 10^5$ $M_\odot$) with ages $\gtrsim$2 Gyr but its presence has not been detected in low-mass systems like Galactic open clusters (e.g. Carrera & Martínez-Vázquez 2013; MacLean, De Silva & Lattanzio 2015) including older ones like NGC 6791 (e.g. Bragaglia et al. 2014; Cunha et al. 2015). The current interpretation for this is that the mechanism responsible for these abundance variations requires high-mass and/or density and/or redshift to operate (see Bastian & Lardo 2018, and references therein). Unfortunately, very little is known about the presence/absence of MPs in low-mass old ($\sim$10 Gyr) stellar clusters. The reason for this is that such systems are very rare, as their chances of getting disrupted/dissolved are very high in these time-scales.

There are approximately ten globular clusters with masses $\lesssim 10^4$ $M_\odot$ (see Baumgardt & Hilker 2018; Vasiliev, Belokurov & Erkal

★ E-mail: eduardo.balbinot@gmail.com

2021). Some of them have been the focus of studies searching for MPs, for example, NGC 6535 and ESO452-SC11 at $\sim 3 \times 10^3\,M_\odot$ and $\sim 8 \times 10^3\,M_\odot$, respectively (see Baumgardt & Hilker 2018; Vasiliev et al. 2021), show some evidence for abundance variations (e.g. Bragaglia et al. 2017; Simpson et al. 2017). On the other hand, in other low-mass globular clusters like E3 ($\sim 3 \times 10^3\,M_\odot$) and Rup 106 ($\sim 3 \times 10^4\,M_\odot$), the presence of MPs has not been detected (e.g. Monaco et al. (e.g. Dotter et al. 2018; Monaco et al. 2018). However, the slopes of their present-day mass functions of these clusters are very shallow/evolved with respect to a Kroupa mass function (see Baumgardt & Hilker 2018; Vasiliev et al. 2021), as is expected for clusters that have suffered a strong dynamical evolution (mass-loss). Understanding the behaviour of MPs in globular clusters in the low end of the globular cluster mass distribution would provide valuable insights into the mechanism responsible for their origin (which remains not very well understood).

The initial mass of cold stellar streams can be more reliably constrained than for MW GCs. This is because the orbit of streams can be accurately measured, and the total number of ejected stars can be estimated from the stream itself, while for GCs, these ejected stars may be present, but too low-mass to be detected. Thus, stellar streams provide a more robust candidate for studying MPs in a truly low-mass regime.

Additionally, the MPs are known to be spatially segregated in many GCs [e.g. Lardo et al. 2011a; Larsen et al. 2015; Dalessandro et al. 2019; Leitinger et al. (in preparation)] and simulations show that the two populations can remain unmixed during most of a GC lifetime (e.g. Hénault-Brunet et al. 2015). If that is the case, the outer population will escape first, leaving this spatial segregation imprinted on the distribution of stream stars. This could be exploited to pinpoint the position of the fully dissolved progenitor, ultimately leading to better dynamical models for stream formation.

The GD-1 stream was discovered using the Sloan Digital Sky Survey (SDSS; Eisenstein et al. 2011) by Grillmair & Dionatos (2006) and in recent years has attracted much attention thanks to the *Gaia* DR2 (Gaia Collaboration et al. 2018), which allowed it to be studied in unprecedented detail (Price-Whelan & Bonaca 2018). Using collisional N-Body simulations, Webb & Bovy (2019) model the dissolution process of GD-1, and conclude that its progenitor must have been a very low-mass GC (a few $10^4\,M_\odot$), that dissolved at most in the last 3 Gyr. Their conclusions would place the progenitor of GD-1 in the low-mass edge of the mass distribution of MW GCs and that the GD-1 progenitor would fully dissolve in a fraction of a Hubble time, possibly pointing to an extragalactic origin or atypically GC evolution/formation. The dynamical mass estimate is supported by observational constraints on the total luminous mass of GD-1 by de Boer, Erkal & Gieles (2020), who report a mass of $1.58 \pm 0.07 \times 10^4\,M_\odot$. The GD-1 location in the outer halo provides a much better case for a truly initially low-mass GC counterpart. We also highlight the recent discovery of evidence for MPs in the Phoenix stream (Balbinot et al. 2016; Wan et al. 2020), with a similarly low mass to GD-1; however, with remarkably low metallicity. The oddities of stellar streams, i.e. their low mass and metallicity, seem to indicate that these objects belong to a distinct class of GCs, perhaps of extra-galactic origins, as discussed previously.

The peculiar characteristics of the GD-1 progenitor place it in a mass-age regime that is not accessible in the present population of GCs. Thus, it is interesting to investigate other properties unique to GCs. As mentioned above, some hypotheses propose that conditions similar to the ones found in the discs of high redshift galaxies (i.e. large gas fractions, high gas densities, and high turbulent speeds) enable the mechanisms responsible for producing the MPs characteristic of GCs (e.g. D'Ercole, D'Antona & Vesperini 2016; Elmegreen 2017; Gieles et al. 2018; Johnson et al. 2019). The implication is that stars that form in low-density environments should not host MPs.

In Section 2, we present the data used to select GD-1 candidate members. In Section 3, we follow up on these candidates and obtain spectra to derive radial velocities, metallicities, and abundance information. In Section 4, we discuss other chemical signatures found in GD-1. And in Section 5, we discuss our results and their implications.

2 DATA

To select GD-1 members, we use the *Gaia* Data Early Release 3 (eDR3; Gaia Collaboration et al. 2020), where we cross-match with LAMOST DR6 [1] (including the subsample from Li et al. 2018), SDSS DR13 photometry (Eisenstein et al. 2011), Pan-STARSS DR1 (Chambers et al. 2016), and 2MASS (Skrutskie et al. 2006). We prefer official *Gaia* cross-matches (Pan-STARRS and 2MASS); however, when not available, we use the Whole Sky Data base (see acknowledgements). For smaller catalogues extracted from literature, we match by *Gaia* eDR3 `source_id` or through a positional match using STILTS (Taylor 2006). We also note that LAMOST has a more recent DR7; however, for comparing our membership selection with literature, we adopt DR6. Later in the paper, we address the newer data.

For the astrometric catalogue of *Gaia* eDR3, we adopted the following quality cut: `RUWE` <1.4 & `visibility_periods_used` >3. We remove some foreground stars using a parallax <1 selection. We limit our catalogue to the reported region occupied by GD-1 as reported by de Boer et al. (2018). All magnitudes in our sample were corrected for extinction using Schlegel, Finkbeiner & Davis (1998) maps and Cardelli, Clayton & Mathis (1989) extinction law, with $R_V = 3.1$.

The LAMOST/SDSS sample from Li et al. (2018) contains multiple observations of some stars. For these duplicates, we compute the average of their line-of-sight velocities and metallicities (when available). Uncertainties were propagated accordingly.

For our analysis, it is useful to define a rotated coordinate system (ϕ_1, ϕ_2) where the equator is approximately aligned with the GD-1. This system is defined via a rotation matrix given by Koposov, Rix & Hogg (2010). We adopt the distances from this same work to correct the proper motions (PMs) for the solar reflex motion. The Schönrich, Binney & Dehnen (2010) reflex motion is used, while the Sun's distance to the Galactic centre is assumed to be 8.3 kpc (Gillessen et al. 2009). We also use the best-fitting 3D position of the stream to bring the stars to a common distance of 8.3 kpc, which is the stream distance at its midpoint. Throughout this paper, we use only distance normalized and de-reddened magnitudes. We also prefer Pan-STARRS magnitudes when not using the *u*-band.

2.1 Membership selection

Following a similar procedure as outlined by Price-Whelan & Bonaca (2018), we define a polygon cut in PM space. This polygon was constructed based on a sample of main-sequence stars selected from a colour–magnitude diagram (CMD) cut and distance to the stream track (as defined by de Boer et al. 2018) less than 2° (i.e. $|\phi_2 - f(\phi_1)| < 2^\circ$; where $f(\phi_1)$ is the interpolated stream track). To

[1] http://dr6.lamost.org/v2.0/

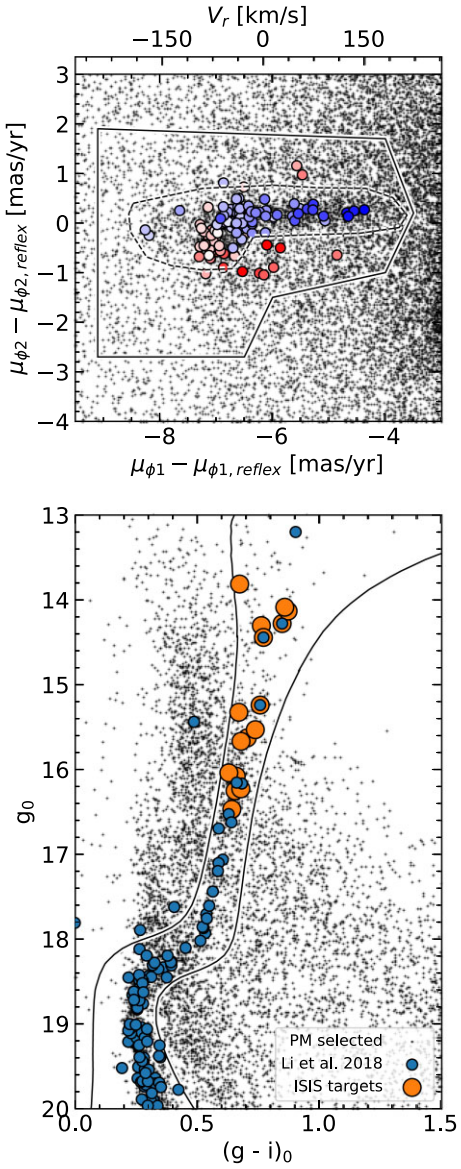

Figure 1. Top panel: PM distribution of CMD selected stars (see panel below) and with $|\phi_2 - f(\phi_1)| < 2°$. The Li, Yanny & Wu (2018) sample is overlaid (blue). The colour scale shows the line-of-sight velocity. Bottom panel: $(g - i)$ *versus* g CMD. The solid lines show a selection based on a PADOVA isochrone of $\log_{10}$age/yr = 10.03 and [Fe/H] = −2.2. We also mark targets that were selected for spectroscopic follow-up (see Section 3).

define a more robust colour–magnitude selection, that includes Red Giant Branch (RGB) stars, we use the PM selected sample and the spectroscopically confirmed sample to define a narrow colour–magnitude cut. When compared to the PM selection from Price-Whelan & Bonaca (2018), or selection is more restrictive, mainly due to RGB stars being brighter, thus having lower astrometric uncertainties. We also note that some spectroscopically confirmed members are not included in our PM selection. These members are typically close to the lower limit in ϕ_1, which was not favoured in our selection due to observability constraints (see Section 3).

In Fig. 1, we show a summary of our selection process. In the top panel, the PM selection polygon is shown, while the sample from Li et al. (2018) is over-plotted. The colour scale indicates the radial velocity value. On the bottom panel, the CMD for the PM-selected sample is shown. To define a CMD selection around likely GD-1 members, we use a PARSEC isochrone (Bressan et al. 2012). Our best-fitting isochrone is defined as the one that well represents the main-sequence and is able to reproduce the observed RGB members from Li et al. (2018). It is out of the scope of this paper to produce a robust isochrone fit, we are interested only in defining a region of the CMD that contains likely GD-1 member stars. For this we defined a range of colours around the best-fitting isochrone based on the photometric uncertainties while allowing for a wider range in colours at bright magnitudes in order to include regions of the CMD where confirmed GD-1 members occupy. When necessary, we also defined colour offsets to our mask to encompass all spectroscopic members of GD-1, except for two likely Blue Stragglers in the Li et al. (2018) sample. In the same Figure, we also defined a new PM selection based on the spectroscopic members, as discussed above.

In the literature, combinations of filters have often been used to pick up the variations in specific spectral features characteristic of the MPs phenomena (e.g. Marino et al. 2008; Lardo et al. 2011b; Monelli et al. 2013). Here, we exploit the C_{ugi} colour index, which is sensitive to CN molecular bands around 385 nm originating from cold stellar atmospheres. This index is defined as:

$$C_{ugi} = (u - g) - (g - i) \quad (1)$$

$$\sigma_{ugi} = \sqrt{\sigma_u^2 + 2\sigma_g^2 + \sigma_i^2}, \quad (2)$$

where σ_{ugi} is the photometric uncertainty propagated from the uncertainties in u, g, and i.

Besides being an indicator for MPs, this colour index is also highly sensitive to metallicity. In Fig. 2 we show the C_{ugi} CMD for stars selected based on PM (narrow selection) and optical CMD (see Fig. 1). We show the CMD for an *on-stream* region (top left-hand panel), defined as $|\phi_2 - f(\phi_1)| < 2°$, and an *off-stream* region (top right-hand panel), defined as $|\phi_2 - f(\phi_1) - 4°| < 2°$. The *off-stream* shows the CMD locus occupied by MW field stars that comply with both our PM and CMD cuts. Based on the best-fitting isochrone, we define a region where contaminants are likely to be found (highlighted in yellow). Notice that due to the uncertainty of the isochrone fit, we allow for a broader range in colour at brighter magnitudes. To confirm that these stars are contaminants, we show their radial velocity distribution as a function of ϕ_1 (i.e. along the stream). When compared to the best-fitting orbit from Koposov et al. (2010) (dashed line), we see that many of the stars have velocities incompatible with the stream. A few stars overlap with the expected velocity trend, but on closer inspection, their metallicity is inconsistent with the bulk of the GD-1 stars (bottom right-hand panel). We find that the C_{ugi} selection is able to remove most of the contaminants, and the few ones left either have incompatible velocities and/or metallicities. We also note the existence of a few LAMOST DR6 stars that could be GD-1 members but that are not in the Li et al. (2018) sample. We follow up on these potential members in the more recent LAMOST DR7 and find that several of these stars have multiple epoch observations. We compute their average spectra, metallicities, and velocities from the LAMOST data base. We select GD-1 members with radial velocities consistent ($< 3\sigma_{V_{los}}$) with the stream orbit and [Fe/H] < -1.75. We use this data in conjunction with the newly obtained spectra presented in the following section.

3 SPECTROSCOPIC FOLLOW-UP

Using the bright high-probability RGB sample defined above, we obtained spectra using the Intermediate-dispersion Spectrograph and

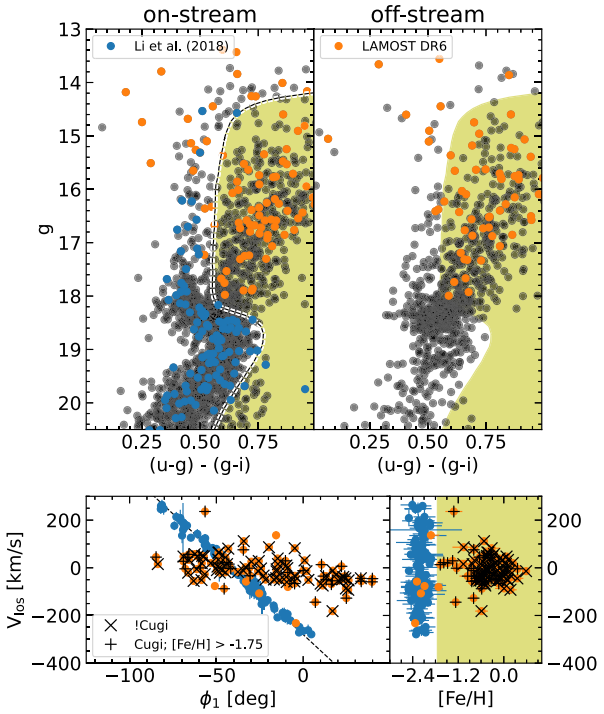

Figure 2. Top left-hand panel: C_{ugi} CMD of the narrow-PM and optical-CMD selected samples. We highlight the Li et al. (2018) (blue) and LAMOST DR6 samples (orange). We overlay the same isochrone used in Fig. 1, shifted in colour (dashed line) to define a selection of potential members. The yellow-shaded region marks the CMD region likely to contain only field stars. Top right: same as the previous panel, but for *off-stream* stars ($|\phi_2 - f(\phi_1) - 4^\circ| < 2^\circ$). Bottom left-hand panel: v_r as a function of ϕ_1, the dashed line is the best-fitting orbit from Koposov et al. (2010). We overplot $\times$ on stars that are likely to be a contaminant based on their position in the C_{ugi} CMD. Stars marked with + signs are removed from the sample since their LAMOST DR6 metallicities do not comply with the bulk of GD-1 stars (bottom right-hand panel).

Imaging System (ISIS) at the 4.2-m William Herschel Telescope (WHT; programme SW2019a05). We use the R300B configuration for the blue-arm, yielding a $R \sim 300$ in the wavelength range of [325, 520] nm. The red-arm was set up in the R1200R mode, yielding a $R \sim 5000$ in the Calcium Triplet spectral region ([830, 890] nm). The exposure time was adjusted such as to yield a S/N of at least 10 at 338 nm in the blue-arm.

We targeted 23 stars based on the membership selection outlined in Section 2.1, these were observed in the course of two nights in 2019 December. Standard long-slit reduction was performed using IRAF, and wavelength calibration was done using CuThAr arc-exposures taken at after each exposure and at the end and beginning of the night. Because of the varying slit losses and the possibility of atmospheric dispersion affecting the spectra towards the blue wavelength, no attempt was made to flux the spectra.

We note that at the time of the observations, only *Gaia* DR2 data were available, and 23 targets were selected for observation, out of which only the 16 higher priority stars were observed due to scheduling and weather. Coincidentally, the stars that were not observed turned out to not pass our selection criteria with the updated *Gaia* eDR3 data. For completeness and compatibility with the observing proposal data, we chose to keep the star ids running from 1 to 23, even though only 16 stars were observed.

We derived the effective temperature and gravity for the stars in our sample with the code BRUTUS,[2] using as input the Pan-STARRS and 2MASS photometry and a prior on the distance coming from the stream track (with 0.5 kpc uncertainties). These values are reported in Table 1 and are the ones used in our analysis of the CN/CH spectral features as well as for the carbon abundances (see Section 3.1).

The radial velocities of the stars in our spectroscopic follow-up were derived from the one-dimensional (1D) reduced and calibrated spectra using `rvspecfit` (Koposov et al. 2011; Koposov 2019) with the PHOENIX V2.0 spectral library (Husser et al. 2013). To obtain reliable uncertainties, we use a Markov chain Monte Carlo minimization that allows for radial velocity, as well as $T_{\rm eff}$, $\log g$, and metallicity to be free. We estimated the best-fitting values as the median of the posterior chains while taking the 25 and 75 percentiles as their respective uncertainties. The radial velocities and stellar parameters derived from this procedure are reported in Table 1. We note that the agreement between the spectroscopic and photometric stellar parameters is very good, and the overall results and conclusions presented below are not dependent on the choice between spectroscopic or photometric $T_{\rm eff}$ and $\log g$.

Although the fitting process described above was applied to spectra from both ISIS arms, we chose to use the red-arm for the velocity and metallicity, since it has higher resolution and allows for a comparison with CaT metallicity determinations. These values can also be found in Table 1. In Fig. 3, we show the method used to select members based on the inferred radial velocity and metallicities. We find that for the 16 *Gaia* eDR3 selected stars observed 13 are likely members based on a [Fe/H] < -1.75 selection alone and find a weighted average metallicity of -2.06 ± 0.10 for this metallicity selected sample. We compare our metallicities to those derived using the CaT equivalent width (Vásquez et al. 2015) and find them to agree within 0.1 dex. When comparing the offset in radial velocity with GD-1 best-fitting orbit, we observe that all low-metallicity stars fall within 2σ ($\sim 7.5\,{\rm km\,s^{-1}}$) of the mean, with the outliers (marked as non-members) being the three highest metallicity stars. We thus conclude that a metallicity selection is sufficient to weed out contaminants in our ISIS sample, as it has already been demonstrated in Fig. 2. The LAMOST DR7 sample was originally constructed using our narrow PM+CMD selection and with added radial velocities, we find that this selection is enough to weed out most contaminants. A single high-metallicity star was identified in this sample and removed from the analysis. We note that the range in ϕ_1 where the three ISIS non-members are located is also where GD-1's orbital line of sight velocity is the most similar to field stars.

In Fig. 4, we show the spatial distribution of high-probability RGB members. Confirmed RGB members from Li et al. (2018) are shown, as well as all the stars where ISIS or LAMOST DR7 spectra is available; however, only the former has labels corresponding to their ID (see Table 1). We limit the spectroscopic samples to the magnitude range of the RGB. We also allow for a fainter selection (black dots), which illustrates the location of the bulk of GD-1's stars.

We find two members in the *spur* region; star #12, which is reported by Li et al. (2018), and #8, which is closer to the main stream track. We also find stars #16, #17, and #23 to be in the region associated the blob/cocoon (Malhan et al. 2018; Price-Whelan & Bonaca 2018). Stars #17, and #23 are the most track deviant GD-1 confirmed members ever detected. We note that very few RGB candidates remain to be followed up in the main body of GD-1,

[2]https://github.com/joshspeagle/brutus

Table 1. IDs, eDR3 `source_id`, rotated coordinates, G-magnitude, blue-arm atmospheric parameters; red-arm radial velocities and metallicity measurements of our targets. Stars in common with Li et al. (2018) and APOGEE DR16 (Ahumada et al. 2020) have their `source_id` marked with an * and †, respectively. We also list the effective temperature ($T_{\rm eff,\,phot}$) and surface gravity ($\log g_{\rm phot}$) derived from photometry (see Section 3). For LAMOST DR7 stars, we list the metallicity and velocity measured by their pipeline, taking their average when multi-epoch data are available.

ID	source_id	ϕ_1	ϕ_2	G	$T_{\rm eff,\,blue}$	$\log g_{\rm blue}$	$T_{\rm eff,\,phot}$	$\log g_{\rm phot}$	$V_{\rm los}$	[Fe/H]
–	–	(deg)	(deg)	(mag)	(K)	(dex)	(K)	(dex)	(km s^{-1})	(dex)
ISIS members										
4	686849456285987840†	−56.31766	0.15197	15.43	5240^{+52}_{-65}	$2.35^{+0.15}_{-0.29}$	5365 ± 38	2.71 ± 0.04	$98.39^{+3.04}_{-3.21}$	$-2.10^{+0.32}_{-0.37}$
6	696138061798355840	−48.90048	−0.26598	14.55	5138^{+15}_{-77}	$1.82^{+0.07}_{-0.65}$	5181 ± 41	2.32 ± 0.05	$49.87^{+0.90}_{-1.08}$	$-2.03^{+0.05}_{-0.07}$
8	796283127046157312	−40.40242	0.71651	15.29	5355^{+38}_{-61}	$2.43^{+0.12}_{-0.26}$	5299 ± 79	2.65 ± 0.06	$-13.31^{+2.86}_{-2.26}$	$-2.31^{+0.33}_{-0.43}$
9	796217426927895168*†	−40.28003	0.13156	13.42	5299^{+5}_{-5}	$2.00^{+0.03}_{-0.01}$	4918 ± 12	1.86 ± 0.06	$-11.75^{+0.54}_{-0.61}$	$-2.00^{+0.02}_{-0.01}$
10	796779998924250624	−38.45281	0.17051	15.56	5255^{+58}_{-68}	$2.03^{+0.30}_{-0.36}$	5395 ± 46	2.80 ± 0.05	$-23.28^{+2.71}_{-3.02}$	$-2.24^{+0.48}_{-0.46}$
12	805475834527735168*	−32.92161	1.13310	13.26	5036^{+6}_{-3}	$1.00^{+0.25}_{-0.05}$	4838 ± 58	1.64 ± 0.05	$-64.71^{+1.08}_{-0.83}$	$-1.97^{+0.10}_{-0.05}$
13	832080270707721088*	−25.31829	0.25339	14.45	5051^{+73}_{-3}	$1.03^{+0.90}_{-0.93}$	5123 ± 62	2.18 ± 0.05	$-114.73^{+0.99}_{-1.22}$	$-2.01^{+0.03}_{-0.05}$
16	840073411003209216	−15.37631	−1.02189	15.13	5164^{+62}_{-101}	$1.62^{+0.27}_{-0.63}$	5216 ± 46	2.44 ± 0.06	$-175.37^{+2.30}_{-1.53}$	$-2.06^{+0.13}_{-0.18}$
17	790916754387404928	−15.85484	−2.62079	14.78	5370^{+35}_{-43}	$2.50^{+0.19}_{-0.19}$	5479 ± 56	2.24 ± 0.06	$-169.52^{+2.12}_{-2.16}$	$-2.19^{+0.21}_{-0.39}$
18	840818192691653504	−12.87469	−0.09236	15.61	5200^{+57}_{-36}	$1.74^{+0.16}_{-0.17}$	5377 ± 31	2.62 ± 0.06	$-190.59^{+2.74}_{-2.26}$	$-2.17^{+0.28}_{-0.43}$
19	840727860939569152	−12.50469	−0.23993	15.14	5252^{+47}_{-54}	$2.35^{+0.18}_{-0.30}$	5291 ± 25	2.42 ± 0.05	$-189.35^{+2.75}_{-2.07}$	$-2.22^{+0.25}_{-0.50}$
20	1573344450075107456	−10.91051	−0.73733	15.65	5394^{+35}_{-44}	$2.50^{+0.16}_{-0.22}$	5382 ± 31	2.65 ± 0.05	$-201.09^{+2.75}_{-2.89}$	$-2.36^{+0.40}_{-0.49}$
23	1576400508285430272	−4.18422	−2.58857	13.72	5038^{+109}_{-3}	$1.02^{+0.97}_{-0.02}$	5000 ± 45	1.67 ± 0.05	$-233.72^{+0.80}_{-0.69}$	$-1.99^{+0.05}_{-0.04}$
ISIS non-members										
1	684655586991056512	−59.94303	1.28547	12.84	5062^{+2}_{-2}	$2.99^{+0.01}_{-0.02}$	4890 ± 55	1.52 ± 0.06	$49.77^{+0.50}_{-0.45}$	$-1.20^{+0.09}_{-0.09}$
2	685227642275283456	−57.91505	0.80182	13.39	5064^{+3}_{-4}	$2.89^{+0.04}_{-0.03}$	4825 ± 25	1.76 ± 0.06	$94.09^{+0.68}_{-0.65}$	$-1.35^{+0.11}_{-0.20}$
11	747560017309217792	−39.49137	−1.97128	13.07	5040^{+3}_{-5}	$2.64^{+0.03}_{-0.04}$	4857 ± 40	1.62 ± 0.06	$-4.39^{+0.60}_{-0.61}$	$-1.53^{+0.08}_{-0.08}$
LAMOST DR7										
–	793009399891751040	−45.78102	0.08422	15.92	–	–	5487 ± 36	2.97 ± 0.04	23.45 ± 8.56	-2.19 ± 0.10
–	793910484031755264*	−44.65316	0.09744	15.62	–	–	5388 ± 60	2.82 ± 0.04	15.11 ± 7.85	-2.23 ± 0.10
–	802849960243599872	−37.86740	0.43362	15.88	–	–	5490 ± 37	2.93 ± 0.05	-27.40 ± 7.14	-2.21 ± 0.10
–	829645264771612800	−27.34517	0.17882	15.99	–	–	5316 ± 50	2.89 ± 0.06	-102.87 ± 6.36	-1.79 ± 0.05
–	832022718144536192*	−22.00954	−0.03175	15.97	–	–	5346 ± 62	2.85 ± 0.06	-142.68 ± 6.86	-2.08 ± 0.13
–	1573762367572774272	−10.41675	−0.24961	15.74	–	–	5002 ± 46	1.67 ± 0.05	-207.65 ± 4.63	-2.30 ± 0.03

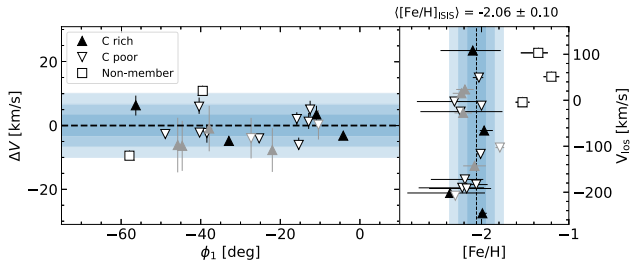

Figure 3. ISIS red-arm radial velocity *versus* ϕ_1 (left) and metallicity (right). Members are marked with up/down triangles depending on their measured C-abundance (see Section 3.1), and non-members are shown as squares. On the left, the velocities have been subtracted by the best-fiting Koposov et al. (2010) orbit. Both panels show the mean (dashed line) as regions 1, 2, and 3σ away from it (shaded blue tones), computed using an uncertainty-weighted average. We note that one of the high-metallicity non-members lies outside of the velocity range in the left-hand panel. In both panels, we show LAMOST DR7 stars in grey, following the same notation as before. These were not used to compute the confidence intervals and average metallicity.

possibly indicating that most RGB belonging to this stream have been found already.

3.1 CN, CH, and carbon abundances

We have calculated the band strengths Sλ3883 (CN) and CHλ4300 (CH) to investigate the presence of multiple populations in GD-1. This technique has been extensively used for GCs in the Galaxy (e.g. Kayser et al. 2008; Martell & Smith 2009; Pancino et al. 2010; Lardo et al. 2013) and clusters in its dwarf satellites (e.g. Hollyhead et al. 2017, 2018, 2019; Martocchia et al. 2021). Indices sensitive to absorption by the 4300 Å CH and the 3883 Å CN bands were measured as described in Norris & Freeman (1979) and Norris et al. (1981).[3] It is extremely difficult to establish a continuum around the 3833 Å CN band, where many atomic and molecular absorption features are present. Thus, no attempt was made to normalize the spectra before computing spectral indices (e.g. Kayser et al. 2008; Pancino et al. 2010). The 4300 Å CH index measurement is independent of this issue as a continuum can be established on both the blue and red sides of the molecular absorption. Errors on measurements are calculated assuming Poisson statistics, following Vollmann & Eversberg (2006). The derived uncertainties reflect the formal statistical uncertainties of the index measurements. Systematic uncertainties are likely higher, but they are not relevant in this context since we are interested in relative differences between band strengths.

In the left-hand panels of Fig. 5, we show the strength of the Sλ3883 (CN) and CHλ4300 (CH) indices as a function of the surface gravity ($\log(g)$) of each star in the ISIS and LAMOST samples (black and grey symbols, respectively). To account for any trend of the indices with atmospheric parameters, we fit a linear model by robust regression – which attempts to down-weight the influence of

[3]The blue-arm ISIS spectra extend to wavelengths where ,in principle, the NH indices could be measured; however, the spectra are of too low S/N at those wavelengths.

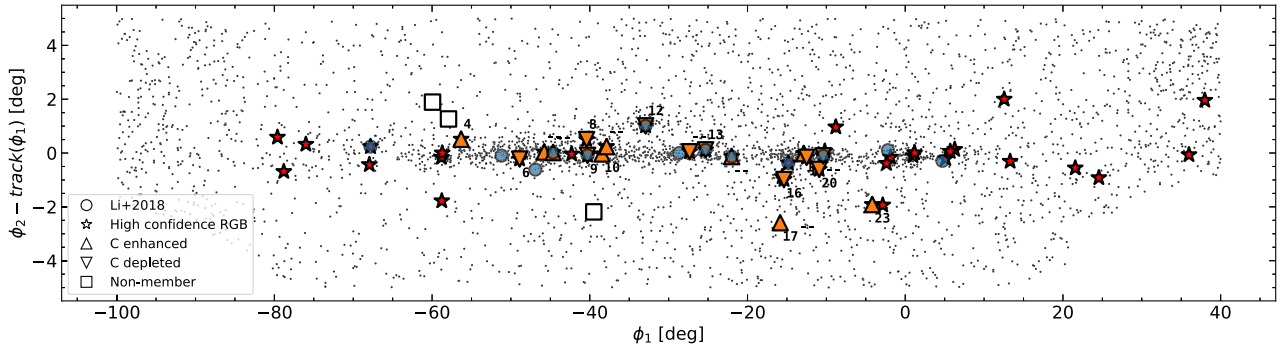

Figure 4. Spatial distributions of CMD (optical and near UV) and PM (narrow) selected stars (black). High probability RGB stars in the magnitude range of $14 < g < 17$ are shown as red stars. We split our spectroscopic sample into three groups: C rich/poor (see Section 3.1) and non-members (see Fig. 3). Stars in our ISIS spectroscopic sample are labelled by their ID (see Table 1). The Li et al. (2018) sample is shown as blue circles.

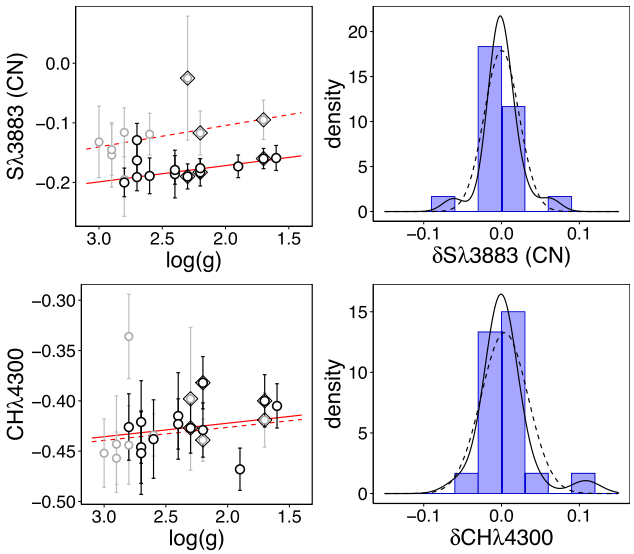

Figure 5. The left-hand panels show the run of the Sλ3883(CN) (top) and CHλ4300 (bottom) indices against the surface gravity (log (g)) for GD1 member stars. Stars from the ISIS and LAMOST data sets are plotted in black and grey, respectively. The solid and dashed red lines indicate the linear fit of those quantities versus magnitude for the ISIS and LAMOST spectra, respectively. Stars with available spectra from both ISIS and LAMOST are indicated with a large diamond. The right-hand panels show the histograms and the associated kernel distributions (solid black line) of the δCN and δCH residuals. The bandwidth of the Gaussian kernel density estimator was selected using the unbiased (least-squares) cross-validation bandwidth selector available in the R package MASS (Venables & Ripley 2002). The dashed line represents the Gaussian distribution that best fits the data.

outliers in order to provide a better fit to the majority of the data (e.g. Venables & Ripley 2002) – between index measurements and log (g). This has been done for the ISIS and LAMOST data sets separately to properly take into account possible offsets between the two data sources sets before analysing and interpreting results. Indeed, while for the CHλ4300 index data from ISIS and LAMOST spectra are on the same scale (see bottom left-hand panel of Fig. 5), this is not the case for the CN index. The top left-hand panel of Fig. 5 shows that the y-intercept of the best-fitting linear model (b_0) is clearly different for the two samples ($b_0 = -0.117 \pm 0.013$ and -0.033 ± 0.044 for ISIS and LAMOST, respectively), whereas its slope is virtually identical. This is likely because the "one-sided" CN index is more sensitive to factors such as e.g. spectral resolution and quality of the flux calibration than the "two-sided" CH index. Differences between the measured Sλ3883 (CN) index from the ISIS and LAMOST spectra are of the order of the ΔSλ3883 (CN)$_{\rm (ISIS-LAMOST)} = -0.65$ mag for both ISIS stars #13 and #23 (stars 832080 and 157640 in LAMOST, respectively), which is comparable to the observed zero-point between the two data sets. A larger difference is observed for ISIS star #6 (star 696138 in LAMOST). However, the index measurements for this star are also characterized by very large errors, so the observed discrepancy is likely due to the lower quality of the LAMOST spectrum.

Indices corrected for temperature and gravity effects (denoted as δCN and δCH) have been obtained by subtracting the robust linear models shown in Fig. 5 from the computed Sλ3883 (CN) and CHλ4300 indices. Their distribution is plotted in the right-hand panels of Fig. 5. In the same panels, the δCN kernel density distribution is also shown along with the best-fitting Gaussian[4]. No evidence for intrinsic δCN and δCH variations that exceed measurement errors can be derived from a careful inspection of the right-hand panels of Fig. 5.

We further investigate the presence of any spreads by modelling the distribution in δCN , and δCH as a 1D normal distribution to our data. Here, we assume that for each data point, a total dispersion can be computed in the form of $\sigma^2 = \sigma_0^2 + \sigma_j^2$, i.e. the sum in quadrature of an intrinsic dispersion and the uncertainty in each j-th data point. We use this distribution to compute a likelihood that is maximized using EMCEE (Foreman-Mackey et al. 2013). We find the intrinsic dispersion of $\sigma_{0,\,\rm CH} = 0.011 \pm 0.008$ for δCH ; and $\sigma_{0,\,\rm CN} = 0.008 \pm 0.007$ for δCN . Both these dispersions are consistent with zero at the 3σ level. Thus, it is not possible to reveal any sign of CN or CH intrinsic variations among GD1 stars from low-resolution spectra.

Although our ISIS spectra do not have the SNR to provide a reliable nitrogen abundance, it was good enough to derive carbon abundances. These were inferred by fitting observed spectra with synthetic ones in the spectral window from 4200 to 4400 Å.

To compute synthetic templates, we adopted the atmospheric parameters and metallicities derived in Section 3 and listed in Table 1. Atomic and molecular line lists were taken from the most recent

[4]To produce histograms and kernel distributions for the *corrected* indices shown in the right-hand panels of Fig. 5 we kept measurements from the ISIS data set only for stars with spectra available in LAMOST.

Kurucz compilation from F. Castelli's website.[5] Model atmospheres were calculated with the ATLAS9 code (Castelli & Kurucz 2004) using the appropriate temperature and surface gravity for each star. We assumed a microturbulent velocity $v_t = 2\,\mathrm{km\,s^{-1}}$ for all the stars. Kurucz's SYNTHE code (Kurucz 2005) was used to produce model spectra. Observed spectra were normalized by using three continuum regions (4200–4275, 4315–4323, and 4350–4440 Å) that are relatively free from large molecular absorption (i.e. changes in carbon absolute abundances of 0.4 dex correspond in these spectral regions to flux variations that are less than 3 per cent). Finally, model spectra with varying carbon abundances were used in a χ^2 minimization with the observed spectra to find the absolute carbon abundances, A(C).

In order to calculate uncertainties from the fit parameters, we iteratively change one parameter by its associated uncertainty and repeat the abundance analysis. Finally, errors introduced by the fitting procedure were estimated by re-fitting a sample of 100 spectra for each star after the introduction of Poissonian noise in the best-fitting template.

In the top panel of Fig. 6, we show absolute carbon abundances A(C) plotted against surface gravity. Increasing carbon depletion with rising luminosity is observed in the data. This can be interpreted as a sign of a mixing process that brings partially processed CN material to the stellar surface when stars evolve along the upper red giant branch (e.g. Sweigart & Mengel 1979; Gratton et al. 2000; Denissenkov & VandenBerg 2003; Martell, Smith & Briley 2008b). Thus, we used the corrections of Placco et al. (2014) to recover the initial carbon abundance of our stars (i.e. carbon abundance not altered by internal stellar mixing). According to Placco et al. (2014), carbon corrections are extremely small (ΔA(C) $\leq$ 0.02) for the majority of the stars analysed here. Larger corrections (spanning values between ΔA(C) = 0.13 − 0.40) are only expected for the three brightest stars in the sample. We list the index measurements and carbon abundances along with their associated uncertainties for all targets in Table 2. In the same table, we also list an evolutionary phase correction for carbon using the results from Placco et al. (2014).

The distribution of the carbon abundances corrected for evolutionary mixing effects, A(C)cor, is shown in the middle panel of Fig. 6 along with its associated kernel distribution and the Gaussian distribution which best fits the data. While most of the stars have A(C)cor values around the median value A(C)cor=6.67 with a small dispersion, there is a clear outlier (star #9) with A(C)cor=5.52 ± 0.07. In the bottom panel of Fig. 6, we show the spectrum of star #9 around the CH absorption at 4300 Å as well as the spectrum of a star with similar atmospheric parameters but a different C abundance (star #12, with A(C)cor=6.49 ± 0.11). The CH band of star #9 looks very weak compared to the stronger absorption observed in star #12. We also show in the same panel the spectra of two fainter objects (star #18 and #20) with nearly identical stellar parameters yet different C content (A(C)cor=6.75 ± 0.09 and A(C)cor=6.51 ± 0.06 for star #18 and #20, respectively). A difference in the CH absorption region is also observed in this case. Visual inspection of the bottom panel of Fig. 6 suggests that the intrinsic variations in carbon abundances may be present in the analysed sample. We define C-rich/poor with respect to the median A(C)cor value and use different symbols to plot C-rich and C-poor stars in the top panel of Fig. 6.

In order to quantitatively assess the presence of an intrinsic spread in carbon, we also repeated our 1-D normal distribution model fit

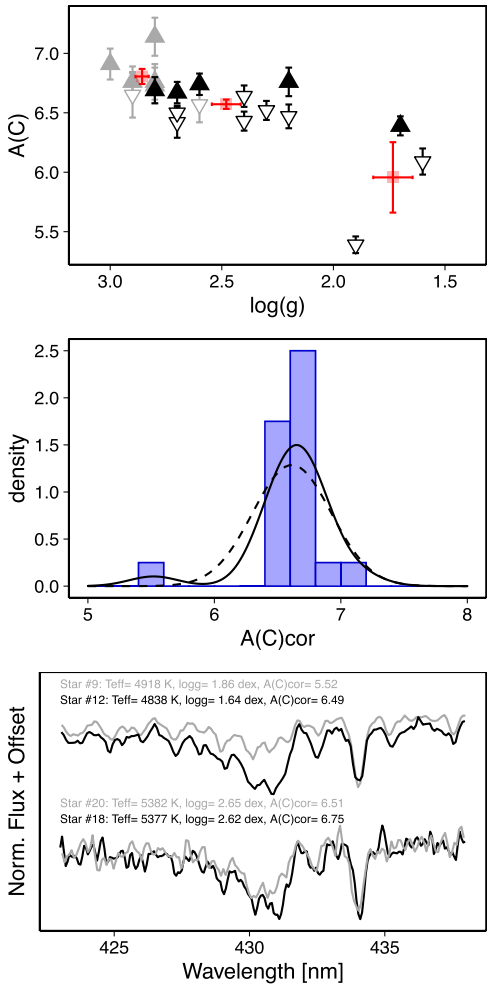

Figure 6. The top panels show the measured absolute carbon abundances A(C) for all red giants in the sample, with stars identified as C-rich/poor with respect to the median A(C)cor value (see text) shown as filled/empty symbols. The three large squares represent the mean and standard error in the luminosity bins: $\log(g) > 2.75$, $2.0 \leq \log(g) \leq 2.75$, and $\log(g) < 2.0$. There is evidence for some deep mixing: stars in the brightest bin have on average lower carbon abundances than fainter stars. The middle panel shows the histograms and the associated kernel distribution (solid black line) of the absolute carbon abundances corrected for evolutionary effects as in Placco et al. (2014). The dashed line represents the Gaussian distribution that best fits the data. The bottom panel shows spectra of stars with similar atmospheric parameters yet very different C content (see legend). C-rich star spectra are in black, whereas the spectra of C-poor stars are plotted in grey.

to the corrected A(C) measurements. This time we find an intrinsic dispersion of $\sigma_{0,C} = 0.32 \pm 0.06$. Given that star #9 is an outlier, we also repeat the fit without it, and find $\sigma_{0,C} = 0.13 \pm 0.04$. This points towards some intrinsic dispersion in the C-abundance of GD-1 stars at a $\sim 3\sigma$ level.

To summarize, we found no statistically significant spreads in the CN and CH indices among the observed RGB stars of GD-1. However, we find evidence for a significant C-abundance spread.

Finally, we note that we found no obvious evidence for a spatial segregation of stars with high/low C-abundance. This is supported by a 2-sample Kolmogorov–Smirnov (KS) test, which suggested that the C-poor and rich populations are drawn from the same distribution in ϕ_1 and $\phi_2 - f(\phi_1)$. This would indicate that GD-1's progenitor was fully mixed by the time it started forming the stream. Although

[5] https://wwwuser.oats.inaf.it/castelli/

Table 2. Measured CH and CN indices, derived carbon abundances and corrections (Placco et al. 2014).

ID –	CN (mag)	CH (mag)	A(C) (dex)	$\Delta A(C)_{corr}$ (dex)
		ISIS		
4	-0.13 ± 0.03	-0.42 ± 0.04	6.67 ± 0.09	0.01
6	-0.19 ± 0.02	-0.43 ± 0.03	6.52 ± 0.08	0.01
8	-0.19 ± 0.02	-0.45 ± 0.04	6.42 ± 0.13	0.01
9	-0.17 ± 0.02	-0.47 ± 0.02	5.39 ± 0.07	0.13
10	-0.20 ± 0.02	-0.43 ± 0.03	6.69 ± 0.11	0.01
12	-0.16 ± 0.02	-0.41 ± 0.02	6.09 ± 0.11	0.40
13	-0.18 ± 0.02	-0.38 ± 0.03	6.47 ± 0.10	0.01
16	-0.18 ± 0.02	-0.42 ± 0.03	6.43 ± 0.08	0.01
17	-0.18 ± 0.02	-0.43 ± 0.03	6.76 ± 0.12	0.01
18	-0.19 ± 0.03	-0.44 ± 0.04	6.74 ± 0.09	0.01
19	-0.19 ± 0.04	-0.42 ± 0.04	6.64 ± 0.09	0.01
20	-0.16 ± 0.03	-0.45 ± 0.04	6.50 ± 0.06	0.01
23	-0.16 ± 0.02	-0.40 ± 0.03	6.39 ± 0.08	0.33
		LAMOST DR7		
696138[a]	-0.03 ± 0.10	-0.40 ± 0.07	6.62 ± 0.13	0.01
793009	-0.13 ± 0.06	-0.45 ± 0.03	6.91 ± 0.13	0.01
793910	-0.12 ± 0.04	-0.44 ± 0.04	6.73 ± 0.15	0.01
802849	-0.15 ± 0.05	-0.44 ± 0.05	6.76 ± 0.13	0.01
829645	-0.15 ± 0.04	-0.46 ± 0.03	6.65 ± 0.19	0.01
832022	-0.20 ± 0.06	-0.34 ± 0.04	7.14 ± 0.16	0.01
832080[b]	-0.12 ± 0.04	-0.44 ± 0.02	6.46 ± 0.14	0.01
157376	-0.12 ± 0.04	-0.43 ± 0.02	6.57 ± 0.15	0.01
157640[c]	-0.10 ± 0.03	-0.42 ± 0.03	6.43 ± 0.14	0.33

Note. [a]star no. 6 in the ISIS sample, [b]star no. 13 in the ISIS sample, and [c]star no. 23 in the ISIS sample.

a deeper and more homogeneous coverage of the stream would be desirable to investigate this further.

4 APOGEE ABUNDANCES

When we crossmatched our sample of bona fide GD-1 RGB candidates with the DR17 catalogue of APOGEE (Majewski et al. 2017; Abdurro'uf et al. 2022), we found two GD-1 stars in common, stars #4 and #9 (both of these also have blue spectra, see Table 1). Overall, the stellar parameters and velocities inferred by APOGEE are consistent with our independent measurements described in the previous sections. Although APOGEE reports C, N, O and Al abundances for these stars (most of the time with small uncertainties), a visual inspection of the APOGEE spectra revealed that even the strongest spectral features that are sensitive to these elements were weak and seriously affected by the noise. Other studies have also cautioned about the reliability of the abundances derived from APOGEE spectra in this temperature/metallicity regime (e.g. Nataf et al. 2019; Mészáros et al. 2020), due to this we will skip these elements in the following discussion.

Unlike the elements mentioned above, the features sensitive to Mg stand out from the noise in the APOGEE spectra, e.g. top panel of Fig. 7. For Mg, APOGEE reports a significant $\sim 3.2\sigma$ difference between the [Mg/Fe] abundances of stars #4 and #9, see Table 3. In particular, star #9, i.e. the star with the lowest C-abundance (see the previous section), is also the one with the lowest [Mg/Fe] as expected in P2 stars in globular clusters (see Charbonnel 2016; Bastian & Lardo 2018; Gratton et al. 2019).

For reference, in the bottom panel of Fig. 7, we compare the Mg-abundances of our GD-1 stars with the ones reported by APOGEE for Galactic GCs of similar metallicities. The average [Mg/Fe] ~ 0.4 dex of these two GD-1 stars is slightly higher than the Galactic clusters, and the difference in abundance between these two GD-1 stars is 0.31 ± 0.10 dex, which is comparable with the scatter observed in Galactic globular clusters. Future studies with larger samples of stars, should be able to quantify this behaviour more robustly.

In summary, the average [Mg/Fe] reported by APOGEE for these GD-1 stars is slightly higher than the one found in Galactic GCs of similar metallicity. Unfortunately, APOGEE only observed two of our GD-1 members; however, the difference in [Mg/Fe] between them is larger than the one expected from the reported uncertainties and spans a similar range to the one observed in globular cluster stars.

5 DISCUSSION AND CONCLUSION

We demonstrate that a selection method using a combination of optical and (near) UV colours is very successful in identifying RGB members of GD-1, selected according to *Gaia* eDR3 PM. In this particular case, we have an 81 per cent success rate, which we attribute to the relatively low metallicity of GD-1, rendering its RGB colour bluer than the bulk of the field population.

We are able to find members associated with off-stream features (*spur* and *blob/cocoon*). We highlight stars #23 and #17, which lie 1.9° and 2.6° away from GD-1 respectively. These two stars are the furthest any confirmed GD-1 member has ever been found. Albeit being far from the stream, we find no significant velocity offset between the literature GD-1 orbit and these off-stream stars. There are several scenarios for the formation of such features (e.g. Erkal, Sanders & Belokurov 2016; Bonaca & Hogg 2018; Malhan et al. 2018), these all predict a very small velocity offset, which is in agreement with what we observe here.

The study of Galactic and M31 globular clusters has revealed that the more massive clusters show stronger signs of abundance variations than low-mass clusters (e.g. Monelli et al. 2013; Schiavon et al. 2013). This is likely a consequence that for the most massive clusters, the fraction of stars with anomalous abundance is larger *and* the magnitude of the abundance variations is stronger (see Milone et al. 2017). The scaling relation between the way the MPs manifest and the mass of a GC could serve as an independent proxy for stream progenitor masses in the future.

Similarly, it has also been shown that for metal-poor GCs, smaller variations in CN are expected as a consequence of the inefficiency to form this molecule (Martell, Smith & Briley 2008a). Both effects combined, i.e. a low $\sim 10^4$ $M_\odot$ mass and low metallicity [Fe/H] ~ -2.1 dex, forecast that any manifestations of the MPs in GD-1 are likely to be subtle.

In our analysis of optical spectra, we find no evidence for a significant spread in CN or CH with the current (large) uncertainties. However, we do find evidence for an intrinsic spread in C-abundances, this detection is significant (at the ~ 99 per cent level) even when we remove star #9, which seems to be an outlier in A(C). We observed no evidence for spatial segregation of stars with different C-abundances in our sample, however, future studies with a more homogeneous coverage of the stream should be able to address this more robustly.

The lack of detectable nitrogen variations in stars with an intrinsic spread in carbon is not surprising. First, double-metal molecules like CN are particularly difficult to observe at the overall low metallicity of GD-1 because their absorption strengths rapidly decline with decreasing metallicity and their formation may be partially inhibited even in the presence of substantial [C/Fe] and [N/Fe] differences (e.g. Sneden 1974; Langer, Suntzeff & Kraft 1992). Secondly, their formation depends both on carbon and nitrogen abundances. Deep

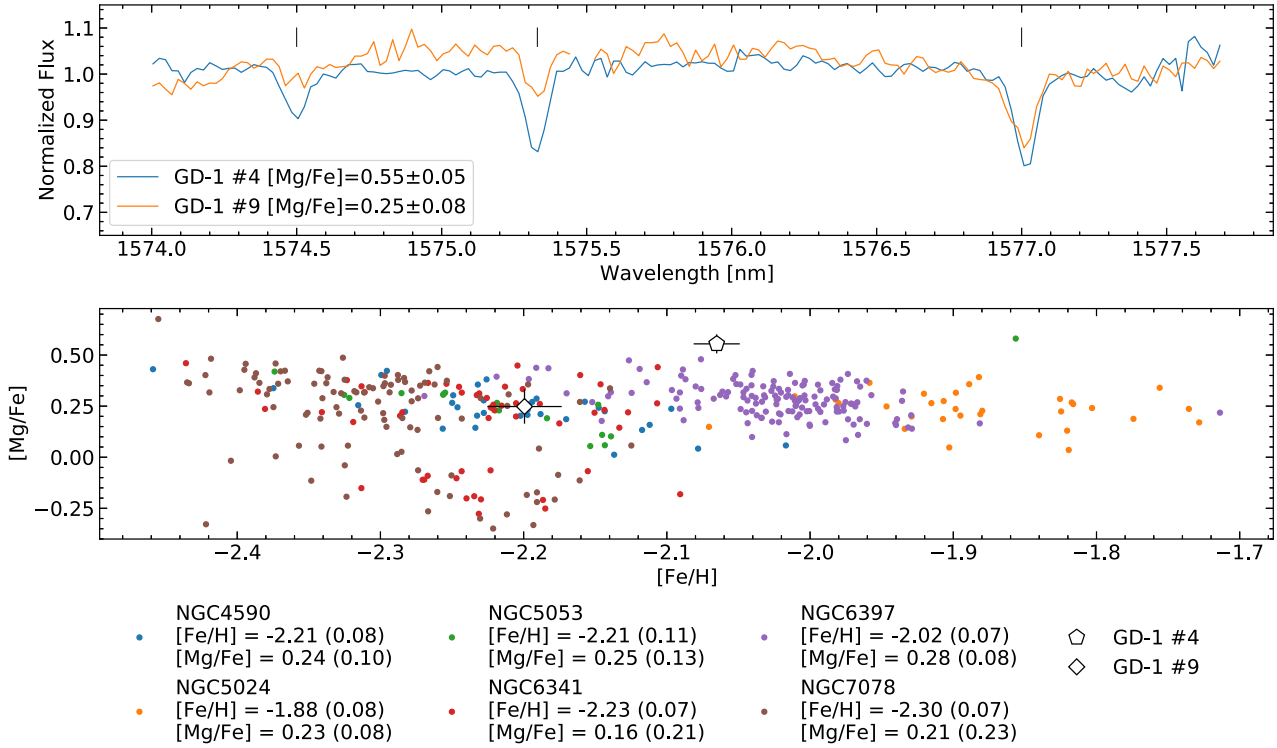

Figure 7. Top panel: APOGEE DR17 spectra of two GD-1 stars around strong Mg lines. Bottom panel: Comparison between the APOGEE [Mg/Fe] of these GD-1 stars and Galactic globular cluster stars of similar metallicity. For each cluster, we quote the mean value of [Fe/H] and [Mg/Fe] and their associated dispersion (standard deviation) in brackets.

Table 3. APOGEE parameters.

ID	$T_{\rm eff}$	log g	$V_{\rm los}$	[Fe/H]	[Mg/Fe]
–	(K)	(dex)	(km s^{-1})	(dex)	(dex)
4	5091 ± 24	2.68 ± 0.07	98.7 ± 0.7	−2.07 ± 0.02	0.55 ± 0.05
9	5068 ± 47	1.96 ± 0.10	− 12.2 ± 0.3	−2.20 ± 0.03	0.25 ± 0.08

mixing scenarios predict that mixing efficiency should be high at low metallicities (e.g. Sweigart & Mengel 1979). Thus, evolved stars in a low-metallicity cluster like GD-1 will also be depleted in carbon and enhanced in nitrogen because of the dredge-up of CNO processed material. If nitrogen becomes more abundant than carbon as a result of this process, the CN band strength no longer scales monotonically with N abundance and can even decline with rising luminosity (e.g. Smith & Bell 1986; Martell et al. 2008a; Lee & Sneden 2021). As a consequence, in the low-metallicity regime, the CN index has only limited sensitivity to variations in nitrogen (see Fig. 9 of Martell et al. 2008a). On the contrary, absorption features of single-metal molecules like CH do not weaken as much with decreasing metallicity, thus they still trace carbon variations at metallicities [Fe/H] < –2.0.

We find that two of our confirmed GD-1 members are in the APOGEE DR17 sample. From these two stars, we found that the mean [Mg/Fe] (∼0.4 dex) is slightly higher than the one found in Galactic GCs of similar metallicities. However, the GD-1 stars show a similar range in [Mg/Fe] (∼0.3 dex) to stars of metal-poor GCs. Moreover, the star with the lowest [Mg/Fe] is also the star for which we inferred the lowest C-abundance (star #9), in agreement with the peculiar chemical patterns found in GC stars. This suggests that GD-1 also manifests the multiple stellar population phenomenon characteristics of more massive, undissolved globular clusters.

If the MPs signal is confirmed, it would make GD-1 another low-mass GC in the [Fe/H] < –2.0 regime to have displayed the phenomena (Ji et al. 2020; Li et al. 2021). This has implications both for the different scenarios for MPs and for the origin of GD-1. In some scenarios (e.g. Elmegreen 2017; Gieles et al. 2018), the formation of MPs is closely tied to a high gas density/pressure environment, thus not allowing for such a low initial mass system as GD-1 to have been formed in those conditions. One could argue that GD-1's initial mass – as inferred by Webb & Bovy (2019) or de Boer et al. (2020) – depends on the mass-loss while orbiting the Galaxy. It is possible that GD-1 belonged to an accreted host galaxy, and had some of its mass striped while in the original host. In this case, it could place it in an initial mass range compatible with Galactic GCs. To confirm the accreted scenario, observing the remnant of the host would be crucial to date the time of accretion and host mass, allowing for stronger constraints on GD-1's initial mass.

Even though *Gaia* helped immensely in the target selection for streams, looking for additional evidence of light element spreads and for the possible host galaxy that brought GD-1 into the Galaxy will be a task for future large-scale high-multiplexing spectroscopic surveys. In the near future, we expect WEAVE (Dalton et al. 2016), to observe all of GD-1's RGB members in high/medium resolution, and provide insight into MPs in this stream and their spatial distribution. Using the same target selection technique used here, we expect to target up to 100 GD-1 members per linear degree in WEAVE's low-resolution halo survey. This work is the first study of the MPs phenomena for a completely dissolved GC, and we show the potential for using streams to open up a new region of parameter space, not available in the local Universe population of GCs.

We also point out that for more metal-rich streams, where the CN band is stronger, they may be promising targets since their RGBs

will split into multiple components in C_{ugi} space, allowing for the study of the distribution of different populations along the stream using photometry alone.

Finally, we would like to mention that our findings support the idea that the small number (a few percent) of halo field stars known to display chemical patterns characteristic of globular cluster stars originated from disrupted/disrupting globular clusters (e.g. Martell et al. 2016; Schiavon et al. 2017; Koch, Grebel & Martell 2019; Hanke et al. 2020; Horta et al. 2021).

ACKNOWLEDGEMENTS

The authors would like to thank Nate Bastian, Mark Gieles, Amina Helmi, Jeremy Webb, and Ricardo Schiavon for the comments and discussions during the early stages of this work. We also thank Tadafumi Matsuno for the insight regarding the APOGEE data and the anonymous referee for the comments and suggestions that helped improve this work.

EB acknowledges support from a Vici grant from the Netherlands Organization for Scientific Research (NWO).

Support for this work was provided by NASA through Hubble Fellowship grant *HST*-HF2-51387.001-A awarded by the Space Telescope Science Institute, which is operated by the Association of Universities for Research in Astronomy, Inc., for NASA, under contract NAS5-26555. This study was supported by the Klaus Tschira Foundation.

CL acknowledges funding from the Ministero dell'Università e della Ricerca through the Programme "Rita Levi Montalcini" (grant PGR18YRML1).

The William Herschel Telescope and its service programme are operated on the island of La Palma by the Isaac Newton Group of Telescopes in the Spanish Observatorio del Roque de los Muchachos of the Instituto de Astrofísica de Canarias.

This work has made use of data from the European Space Agency (ESA) mission *Gaia* (https://www.cosmos.esa.int/gaia), processed by the *Gaia* Data Processing and Analysis Consortium (DPAC, https://www.cosmos.esa.int/web/gaia/dpac/consortium). Funding for the DPAC has been provided by national institutions, in particular the institutions participating in the *Gaia* Multilateral Agreement.

Funding for SDSS-III has been provided by the Alfred P. Sloan Foundation, the Participating Institutions, the National Science Foundation, and the U.S. Department of Energy Office of Science. The SDSS-III web site is http://www.sdss3.org/.

The SDSS-III is managed by the Astrophysical Research Consortium for the Participating Institutions of the SDSS-III Collaboration, including the University of Arizona, the Brazilian Participation Group, Brookhaven National Laboratory, Carnegie Mellon University, University of Florida, the French Participation Group, the German Participation Group, Harvard University, the Instituto de Astrofisica de Canarias, the Michigan State/Notre Dame/JINA Participation Group, Johns Hopkins University, Lawrence Berkeley National Laboratory, Max Planck Institute for Astrophysics, Max Planck Institute for Extraterrestrial Physics, New Mexico State University, New York University, Ohio State University, Pennsylvania State University, University of Portsmouth, Princeton University, the Spanish Participation Group, University of Tokyo, University of Utah, Vanderbilt University, University of Virginia, University of Washington, and Yale University.

The Guoshoujing Telescope (the Large Sky Area Multi-Object Fiber Spectroscopic Telescope, LAMOST) is a National Major Scientific Project built by the Chinese Academy of Sciences. Funding for the project has been provided by the National Development and Reform Commission. LAMOST is operated and managed by the National Astronomical Observatories, Chinese Academy of Sciences. This paper made use of the Whole Sky Data base (wsdb) created by Sergey Koposov and maintained at the Institute of Astronomy, Cambridge by Sergey Koposov, Vasily Belokurov, and Wyn Evans with financial support from the Science & Technology Facilities Council (STFC) and the European Research Council (ERC).

The following software packages were used in this publication: ASTROPY (Astropy Collaboration et al. 2013; Price-Whelan et al. 2018), GALA (Price-Whelan 2017), IPYTHON (Pérez & Granger 2007), MATPLOTLIB (Hunter 2007), NUMPY (Walt, Colbert & Varoquaux 2011), SCIPY (Jones et al. 2001), and VAEX (Breddels & Veljanoski 2018)

DATA AVAILABILITY

All the survey data used in the work are publicly available. The reduced data underlying this work are available from the authors upon reasonable request.

REFERENCES

Abdurro'uf et al., 2022, ApJS, 259, 35
Ahumada R. et al., 2020, ApJS, 249, 3
Astropy Collaboration et al., 2013, A&A, 558, A33
Balbinot E. et al., 2016, ApJ, 820, 58
Bastian N., Lardo C., 2018, ARA&A, 56, 83
Baumgardt H., Hilker M., 2018, MNRAS, 478, 1520
Bernard E. J. et al., 2016, MNRAS, 463, 1759
Bonaca A., Hogg D. W., 2018, ApJ, 867, 101
Bragaglia A., Carretta E., D'Orazi V., Sollima A., Donati P., Gratton R. G., Lucatello S., 2017, A&A, 607, A44
Bragaglia A., Sneden C., Carretta E., Gratton R. G., Lucatello S., Bernath P. F., Brooke J. S. A., Ram R. S., 2014, ApJ, 796, 68
Breddels M. A., Veljanoski J., 2018, A&A, 618, A13
Bressan A., Marigo P., Girardi L., Salasnich B., Dal Cero C., Rubele S., Nanni A., 2012, MNRAS, 427, 127
Cardelli J. A., Clayton G. C., Mathis J. S., 1989, ApJ, 345, 245
Carrera R., Martínez-Vázquez C. E., 2013, A&A, 560, A5
Castelli F., Kurucz R. L., 2004, A&A, 419, 725
Chambers K. C. et al., 2016, preprint (arXiv:1612.05560)
Charbonnel C., 2016, in Moraux E., Lebreton Y., Charbonnel C., eds, Stellar Clusters: Benchmarks of Stellar Physics and Galactic Evolution - EES2015, Vol. 80-81, EAS Publications Series, p. 177,
Cunha K. et al., 2015, ApJ, 798, L41
D'Ercole A., D'Antona F., Vesperini E., 2016, MNRAS, 461, 4088
Dalessandro E. et al., 2019, ApJ, 884, L24
Dalton G. et al., 2016, in Skillen Balcells M., Trager S., eds, ASP Conf. Ser. Vol. 507, Proceedings of Multi-Object Spectroscopy in the Next Decade: Big Questions, Large Surveys, and Wide Fields, Astron. Soc. Pac., San Francisco, p. 97
de Boer T. J. L., Belokurov V., Koposov S. E., Ferrarese L., Erkal D., Côté P., Navarro J. F., 2018, MNRAS, 477, 1893
de Boer T. J. L., Erkal D., Gieles M., 2020, MNRAS, 494, 5315
Denissenkov P. A., VandenBerg D. A., 2003, ApJ, 593, 509
Dotter A., Milone A. P., Conroy C., Marino A. F., Sarajedini A., 2018, ApJ, 865, L10
Eisenstein D. J. et al., 2011, AJ, 142, 72
Elmegreen B. G., 2017, ApJ, 836, 80
Erkal D., Sanders J. L., Belokurov V., 2016, MNRAS, 461, 1590
Foreman-Mackey D., Hogg D. W., Lang D., Goodman J., 2013, PASP, 125, 306
Gaia Collaboration et al., 2020, A&A, 649, A1
Gaia Collaboration, Brown A. G. A., Vallenari A., Prusti T., de Bruijne J. H. J., Babusiaux C., Bailer-Jones C. A. L., 2018, A&A, 616, A1
Gieles M. et al., 2018, MNRAS, 478, 2461

Gieles M., Erkal D., Antonini F., Balbinot E., Peñarrubia J., 2021, Nat. Astron., 5, 957
Gillessen S., Eisenhauer F., Trippe S., Alexand er T., Genzel R., Martins F., Ott T., 2009, ApJ, 692, 1075
Gratton R. G., Sneden C., Carretta E., Bragaglia A., 2000, A&A, 354, 169
Gratton R., Bragaglia A., Carretta E., D'Orazi V., Lucatello S., Sollima A., 2019, A&A Rev., 27, 8
Grillmair C. J., Dionatos O., 2006, ApJ, 643, L17
Hanke M., Koch A., Prudil Z., Grebel E. K., Bastian U., 2020, A&A, 637, A98
Hénault-Brunet V., Gieles M., Agertz O., Read J. I., 2015, MNRAS, 450, 1164
Hollyhead K. et al., 2017, MNRAS, 465, L39
Hollyhead K. et al., 2018, MNRAS, 476, 114
Hollyhead K. et al., 2019, MNRAS, 484, 4718
Horta D. et al., 2021, MNRAS, 500, 5462
Hunter J. D., 2007, Comput. Sci. Eng., 9, 90
Husser T. O., Wende-von Berg S., Dreizler S., Homeier D., Reiners A., Barman T., Hauschildt P. H., 2013, A&A, 553, A6
Ibata R. A., Malhan K., Martin N. F., 2019, ApJ, 872, 152
Ji A. P. et al., 2020, AJ, 160, 181
Johnson C. I., Caldwell N., Michael Rich R., Mateo M., Bailey J. I., 2019, MNRAS, 485, 4311
Kayser A., Hilker M., Grebel E. K., Willemsen P. G., 2008, A&A, 486, 437
Koch A., Grebel E. K., Martell S. L., 2019, A&A, 625, A75
Koposov S. E. et al., 2011, ApJ, 736, 146
Koposov S. E., 2019, Astrophysics Source Code Library, record ascl:1907.013
Koposov S. E., Rix H.-W., Hogg D. W., 2010, ApJ, 712, 260
Küpper A. H. W., Balbinot E., Bonaca A., Johnston K. V., Hogg D. W., Kroupa P., Santiago B. X., 2015, ApJ, 803, 80
Kurucz R. L., 2005, Mem. Soc. Astron. Ital. Suppl., 8, 14
Kuzma P. B., Da Costa G. S., Mackey A. D., 2018, MNRAS, 473, 2881
Langer G. E., Suntzeff N. B., Kraft R. P., 1992, PASP, 104, 523
Lardo C. et al., 2013, MNRAS, 433, 1941
Lardo C., Bellazzini M., Pancino E., Carretta E., Bragaglia A., Dalessandro E., 2011a, A&A, 525, A114
Lardo C., Bellazzini M., Pancino E., Carretta E., Bragaglia A., Dalessandro E., 2011b, A&A, 525, A114
Larsen S. S., Baumgardt H., Bastian N., Brodie J. P., Grundahl F., Strader J., 2015, ApJ, 804, 71
Lee J.-W., Sneden C., 2021, ApJ, 909, 167
Li G.-W., Yanny B., Wu Y., 2018, ApJ, 869, 122
Li T. S. et al., 2021, ApJ, 911, 149
MacLean B. T., De Silva G. M., Lattanzio J., 2015, MNRAS, 446, 3556
Majewski S. R. et al., 2017, AJ, 154, 94
Malhan K., Ibata R. A., Martin N. F., 2018, MNRAS, 481, 3442
Marino A. F., Villanova S., Piotto G., Milone A. P., Momany Y., Bedin L. R., Medling A. M., 2008, A&A, 490, 625
Martell S. L. et al., 2016, ApJ, 825, 146
Martell S. L., Smith G. H., 2009, PASP, 121, 577
Martell S. L., Smith G. H., Briley M. M., 2008a, PASP, 120, 7
Martell S. L., Smith G. H., Briley M. M., 2008b, AJ, 136, 2522
Martocchia S. et al., 2021, MNRAS, 505, 5389
Massari D., Koppelman H. H., Helmi A., 2019, A&A, 630, L4
Mészáros S. et al., 2020, MNRAS, 492, 1641
Milone A. P. et al., 2017, MNRAS, 464, 3636
Monaco L., Villanova S., Carraro G., Mucciarelli A., Moni Bidin C., 2018, A&A, 616, A181
Monelli M. et al., 2013, MNRAS, 431, 2126
Nataf D. M. et al., 2019, AJ, 158, 14
Norris J., Cottrell P. L., Freeman K. C., Da Costa G. S., 1981, ApJ, 244, 205
Norris J., Freeman K. C., 1979, ApJ, 230, L179
Odenkirchen M. et al., 2001, ApJ, 548, L165
Pancino E., Rejkuba M., Zoccali M., Carrera R., 2010, A&A, 524, A44
Pérez F., Granger B. E., 2007, Comput. Sci. Eng., 9, 21
Placco V. M., Frebel A., Beers T. C., Stancliffe R. J., 2014, ApJ, 797, 21
Price-Whelan A. M. et al., 2018, AJ, 156, 123
Price-Whelan A. M., 2017, J. Open Source Softw., 2, 388
Price-Whelan A. M., Bonaca A., 2018, ApJ, 863, L20
Schiavon R. P. et al., 2017, MNRAS, 465, 501
Schiavon R. P., Caldwell N., Conroy C., Graves G. J., Strader J., MacArthur L. A., Courteau S., Harding P., 2013, ApJ, 776, L7
Schlegel D. J., Finkbeiner D. P., Davis M., 1998, ApJ, 500, 525
Schönrich R., Binney J., Dehnen W., 2010, MNRAS, 403, 1829
Shipp N., Drlica-Wagner A., Balbinot E., DES Collaboration, 2018, AAS Meeting Abstracts, #231
Simpson J. D., De Silva G., Martell S. L., Navin C. A., Zucker D. B., 2017, MNRAS, 472, 2856
Skrutskie M. F. et al., 2006, AJ, 131, 1163
Smith G. H., Bell R. A., 1986, AJ, 91, 1121
Sneden C., 1974, ApJ, 189, 493
Sollima A., 2020, MNRAS, 495, 2222
Sweigart A. V., Mengel J. G., 1979, ApJ, 229, 624
Taylor M. B., 2006, in Gabriel C., Arviset C., Ponz D., Enrique S., eds, ASP Conf. Ser. Vol. 351, Astronomical Data Analysis Software and Systems XV, Astron. Soc. Pac., San Francisco, p. 666
Vasiliev E., Belokurov V., Erkal D., 2021, MNRAS, 501, 2279
Vásquez S., Zoccali M., Hill V., Gonzalez O. A., Saviane I., Rejkuba M., Battaglia G., 2015, A&A, 580, A121
Venables W. N., Ripley B. D., 2002, Modern Applied Statistics with S, 4 edn. Springer, New York, NY, https://www.stats.ox.ac.uk/pub/MASS4/
Virtanen et al., 2020, Nature Methods, 17, 261 http://www.scipy.org/
Vollmann K., Eversberg T., 2006, Astron. Nachr., 327, 862
Walt S. V. D., Colbert S. C., Varoquaux G., 2011, Comput. Sci. Eng., 13, 22
Wan Z. et al., 2020, Nature, 583, 768
Webb J. J., Bovy J., 2019, MNRAS, 485, 5929

This paper has been typeset from a TEX/LATEX file prepared by the author.